Available online at www.sciencedirect.com

ScienceDirect

Procedia Computer Science 217 (2023) 928–937

Procedia Computer Science

www.elsevier.com/locate/procedia

4th International Conference on Industry 4.0 and Smart Manufacturing

Computational evaluation of the compressive properties of different lattice geometries to be used as temporary implants

Pedro Nogueira[a]*, Kerman Castresana[b], J.Magrinho[a], M.Beatriz Silva[a], Augusto Moita de Deus[c], M.Fátima Vaz[a]

[a] *IDMEC, Dept. Mechanical Engineering, Instituto Superior Técnico, Universidade de Lisboa, Av. Rovisco Pais, 1 1049-001, Lisbon, Portugal*
[a] *Mondragon Unibertsitatea, Faculty of Engineering Mechanics and Industrial Production, Loramendi 4, Mondragon 20500, Gipuzkoa, Spain*
[c] *CeFEMA, Dept. Mechanical Engineering, Instituto Superior Técnico, Universidade de Lisboa, Av. Rovisco Pais, 1 1049-001, Lisbon, Portugal*

Abstract

Additive manufactured iron lattice structures present unprecedented capabilities for fulfilling the role of bone temporary implants. Iron structures are biodegradable, eliminating the need for removal surgeries, and can help reduce stress shielding significantly by mimicking the properties of bone locally. Although several types of lattice structures have been proposed in the literature, there is the need to evaluate the effect of the relative density on their mechanical properties, in order to resemble bone properties.

In the present work, the effects of relative density on the mechanical behavior and in particular, in elastic mechanical properties, were evaluated with finite element simulations, for several types of cells.

Lattices, i.e, arrays of unit cells, were designed for 5% increments of relative density, from 5% up to the maximum allowed for each specific cell, for 5 different cell types, creating a total of 63 lattice structures. Finite element models were created for each geometry simulating a compression test, obtaining stress-strain curves and thus the Young's modulus. The material data introduced in the finite element analysis was obtained experimentally from a compression test on bulk iron.

The results suggest that all lattice structures evaluated were stable for high density. Cubic (C), truncated cubic (TC), and rhombicuboctahedron (RCO) cells presented instability at low densities while truncated octahedron (TO) and rhombitruncated cuboctahedron (RTCO) cells remained stable at low densities, reaching the value of the Young's modulus of very low-density trabecular bone.

Two cell types, RTCO and TO, showed the ability to reproduce the whole range of mechanical properties of bone in a stable manner. The other cell types experienced instability phenomena, like buckling, at low densities.

* Corresponding author. Tel.: +218417340.
E-mail address: pedro.ferreira.nogueira@tecnico.ulisboa.pt

1877-0509
10.1016/j.procs.2022.12.290

Keywords: Lattice strutures; stress shielding; biodegradable; temporary implants; iron; relative density; Young's modulus

1. Introduction

Temporary implants can be made of biodegradable metals. This allows implants to be absorbed by the body, with no need for a removal surgery. The mechanical properties and degradation rate of biodegradable metals make it inadequate to use the bulk material for this end. So, lattice structures can be employed, tuning the degradation rate and the mechanical properties of the implants, making them more similar to the properties required to mimic the human body. Lattice structures have a complex geometry that cannot be manufactured with traditional manufacturing techniques, therefore these structures are usually manufactured by additive manufacturing (AM). Additive manufactured biometals have recently been a focus of research [1] as they present unprecedented opportunities for developing patient-specific solutions for bone implants. AM porous metal scaffolds open the possibility of mimicking the bone's mechanical properties, reducing stress-shielding, while enabling bone ingrowth and the biodegradation of the scaffold itself [2].

There are three metals and their alloys that show promising capabilities of fulfilling the role of temporary implants whilst being biodegradable, completely absorbable by the human body without creating further complications: iron [3], magnesium, and zinc [4–7]. Magnesium offers a good capability of reproducing the bone's mechanical properties, however its degradation products contain hydrogen bubbles that can be harmful and it has a high degradation rate and so, the lattice structure degrades way before the host can heal [3,8]. Zinc, on the other hand, has the adequate degradation rate but lacks the mechanical properties to provide bone support, i.e., the material is not stiff enough [3,4]. Iron has mechanical properties such as stiffness that are much higher than bone and a degradation rate that is too slow. However, it seems to be the most interesting of the three metals to employ in lattice structures as the reduction in density promotes lower mechanical properties, e.g. Young's modulus, and higher surface area compared with its bulk counterpart. This enables its mechanical properties to reach the required values to mimic those of both trabecular and cortical bone and the degradation rate that is adequate for bone healing [3,4,8,9]. Bearing this in mind, iron is the material used in the lattice structures of this study.

The lattice structures are cellular materials composed of a repetition of unit cells, and a large variety of them have been studied regarding their mechanical properties [10–12] and degradation rate [3,10,13]. These properties are heavily dependent on the cell geometry: the load bearing capabilities of the cells are dependent on the geometry and the degradation rate is dependent on the surface area, that is a function of the geometry. The work of Ahmadi et al. (2015) [11] suggests that diamond cells present the lowest mechanical properties and raises the problem of the geometric accuracy that can be achieved in selective laser melting (SLM), as deviations between the design and the production are high. Chantarapanich et al. (2012) [12] have studied the geometry of 119 polyhedrons, concluding that only 6 open-cell polyhedrons are proper candidates for lattice structures.

This study aims to evaluate how the elastic mechanical properties of different unit cell geometries vary with their relative density ($\bar{\rho}$), to best mimic the properties of bone, thus minimizing stress-shielding. Five cell geometries were selected to be featured in this study: Cubic (C), Truncated Octahedron (TO), Truncated Cubic (TC), Rhombicuboctahedron (RCO) and Rhombitruncated Cuboctahedron (RTCO). To this end, the stress-strain curves obtained from compressive tests done with finite element models were analyzed to characterize the structures' behavior under compression. Additionally, some geometric considerations about the cell types are done and possible instabilities that occur in very low-density cells are evaluated.

2. Materials and methods

2.1. Geometry and relative density analysis

Five lattice geometries were modeled, with different unit cells, in Solid Edge 2020 (SIEMENS, Munich, Germany): Cubic (C), Truncated Octahedron (TO), Truncated Cubic (TC), Rhombicuboctahedron (RCO), and Rhombitruncated Cuboctahedron (RTCO) (Fig. 1). Each cell has outer dimensions that fit in a cube of 3.5 mm in length. For the finite element models, assemblies for each cell type were created containing 8 cells assembled in a 2x2x2 fashion, as detailed in Fig. 1.

For each cell type, the relative density ($\bar{\rho}$) is equivalent to the ratio between the volume occupied by the material ($V_{material}$) and the entire volume (V) [14]. So, $\bar{\rho}$ varies from 0 to 1 and is defined as:

$$\bar{\rho} = \frac{V_{material}}{V} \tag{1}$$

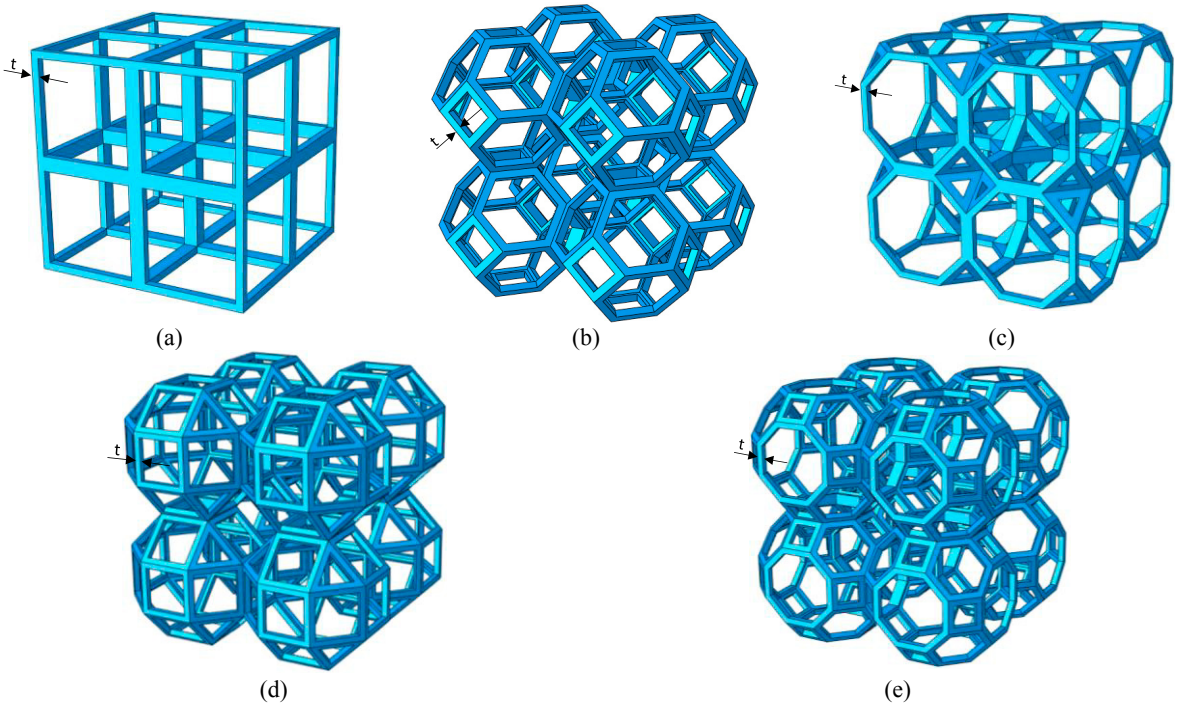

Fig. 1. Geometry of the 2x2x2 assemblies with 5% relative density: (a) Cubic, (b) Truncated Octahedron, (c) Truncated Cubic, (d) Rhombicuboctahedron and (e) Rhombitruncated Cuboctahedron. t – strut thickness is indicated with black arrows.

For each cellular structure considered, the density is varied by changing the strut thickness (t), Fig. 1. Therefore, for each cell type, there is a limit of density that can be achieved as the different cell types become impossible to manufacture when the strut thickness increases and creates enclosed pores [12]. Enclosed pores can't be manufactured in SLM because the powder within the pore cannot be removed. Fig. 2 illustrates this phenomenon with TO cells of different relative densities. Fig. 2 (a) shows TO cells with a relative density of 5.0% that depicts the geometry of this cell type, as the strut thickness increases and the relative density changes to 29,7% in Fig. 2 (b), some of the faces are filled, decreasing the number of holes. In Fig. 2 (c) with a 45.0% relative density, the last increment in density that does not generate an enclosed pore is shown. A 50% relative density would fill all surfaces and create an enclosed pore within each cell, making it impossible to manufacture with SLM.

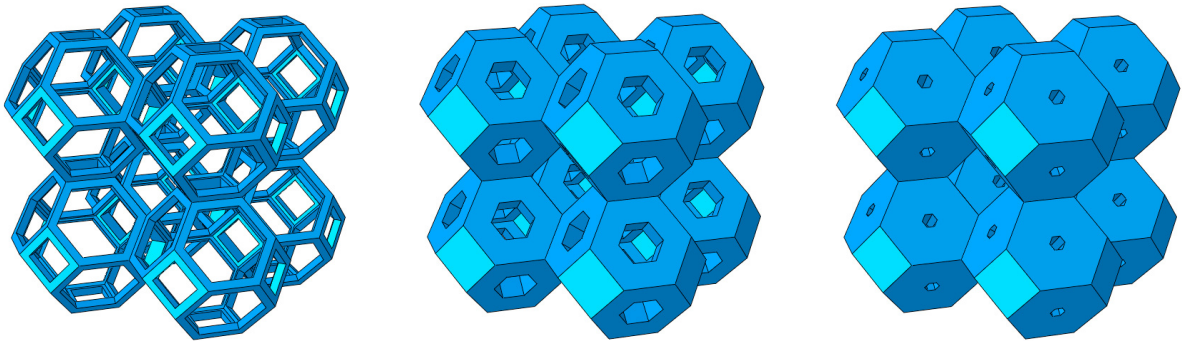

Fig. 2. TO cells with different relative densities: (a) 5.0%, (b) 29.7% and (c) 45.0%.

A model of every structure was obtained approximately every 5% of relative density, from 5% up to 80%, or the maximum for that specific structure. The relative density was not increased further than 80% as with this relative density the cells are too close to the bulk material and, therefore, have mechanical properties much higher than necessary to mimic trabecular and cortical bone. As the density was obtained by varying the strut thickness and there are issues with enclosed pores, the values of density are not always round numbers and may have small deviations.

2.2. Material characterization

The material properties of iron with 99.8% purity, from Goodfellow Inc., Cambridge, UK, were obtained experimentally through compression tests performed in an Instron SATEC 1200, with a load cell of 1200 kN, according to ASTM E9-19 (ASTM, 2019). The tests were performed at a constant speed of 2.5 mm/min in C1 type specimens that were cut from a pure iron rod to have the desired dimensions that are specified in the standard. The Ludwik-Hollomon curve was obtained, equation 2.

$$\bar{\sigma} = 941.41\bar{\varepsilon}^{0.216} \tag{2}$$

where, $\bar{\sigma}$ (MPa) is the true stress and $\bar{\varepsilon}$ is the true plastic strain.

2.3. Finite element modeling

A finite element model was developed in Abaqus 2021 (Dassault Systèmes, Waltham, MA, USA) for every cell type and every $\bar{\rho}$ described previously. Table 1 shows every relative density considered.

The formulation used was Dynamic Implicit in Abaqus/Standard, that is suitable for solving smooth non-linear problems. The various arrays of cells were compressed between two rigid surfaces: the support and the punch. No loads were directly applied to the cells, instead the boundary conditions consisted of moving the punch 1 mm at a constant speed of 2.1 mm/min towards the support, that was fixed, compressing the specimen. The punch speed was chosen in a way that the deformation rate was within the bounds imposed by the standard ISO 13314:2011(E) [16]. The interaction between the cells and the tools (punch and support) was modeled with a Coulomb friction coefficient of 0.05, simulating a condition in which there is a thin Teflon layer between the cellular structure and the surfaces of the testing machine. The output requested was the reaction force on the support and the engineering stresses were computed for each output point. Given that this work focuses more on the elastic properties, there was a need to increase the accuracy in this region, requesting more output points of the stress-strain curve, thus ensuring higher accuracy in the Young's modulus calculation. The high number of points could not be maintained in the plastic regime to ensure a low computational cost.

Following the material characteristics tested, the structures are made of iron with a Young's modulus of 200 GPa and a Poisson's ratio of 0.29. Also, the plastic regime of the material was considered by introducing in Abaqus the

data from the experimental stress-strain curve obtained for the material characterization.

The mesh was made of quadratic tetrahedral elements (C3D10). A mesh convergence analysis was done in which the stress-strain curve was analyzed, concluding that a 0.3 mm average size for the mesh was enough to obtain satisfactory results in cells with densities above 15%, and a 0.15 mm average size for cells with densities of 15% or lower. Fig. 3 shows an example of the meshes of RTCO cells for 10.3% (Fig. 3a) and 29.9% (Fig. 3b) of relative density.

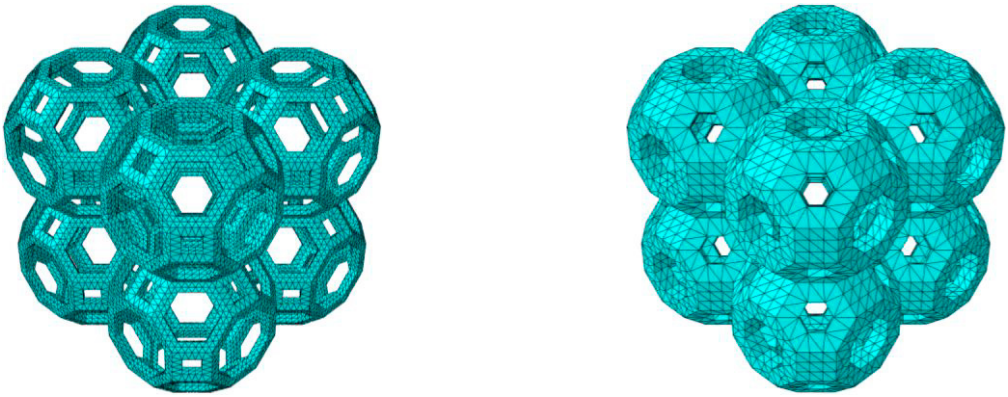

Fig. 3. Finite element models' mesh for RTCO cells with a relative density of (a) 10.3% and (b) 29.9%

For each cell geometry a finite element model was developed with the same modeling conditions according to the description in this section.

2.4. Data analysis

To compare the elastic mechanical properties of the lattice structures with those of bone available in the literature, the elastic material properties of the structures must be computed.

With the points from the stress-strain curves obtained with the numeric simulations, the Young's modulus was computed with a MATLAB code (version 2018a) that used the first three points of the elastic regime to make a linear regression. The Young's modulus was the slope of the linear regression.

3. Results and discussion

From the various relative density values considered for each geometry, a total of 63 finite element models were studied. In this section, the stress-strain curve of all models is analyzed along with their three-dimensional deformation behavior and the elastic mechanical properties.

3.1. Stress-strain curves

For each of the 63 models, a stress-strain curve was obtained. Fig. 4 shows the results for cubic and RTCO cells. For briefness, not all stress-strain curves are presented. Fig. 4 (a) exhibits all the results for cubic cells and (b) shows the same results but only for relative densities between 5% and 30%. Fig. 4 (c) presents all the results for RTCO cells and (d) shows the same results but only for relative densities between 5% and 30%. Fig. 4 (b) and (d) enhance the detail of the stress-strain curves at low density, that allows for a more detailed analysis of the deformation behavior at low density.

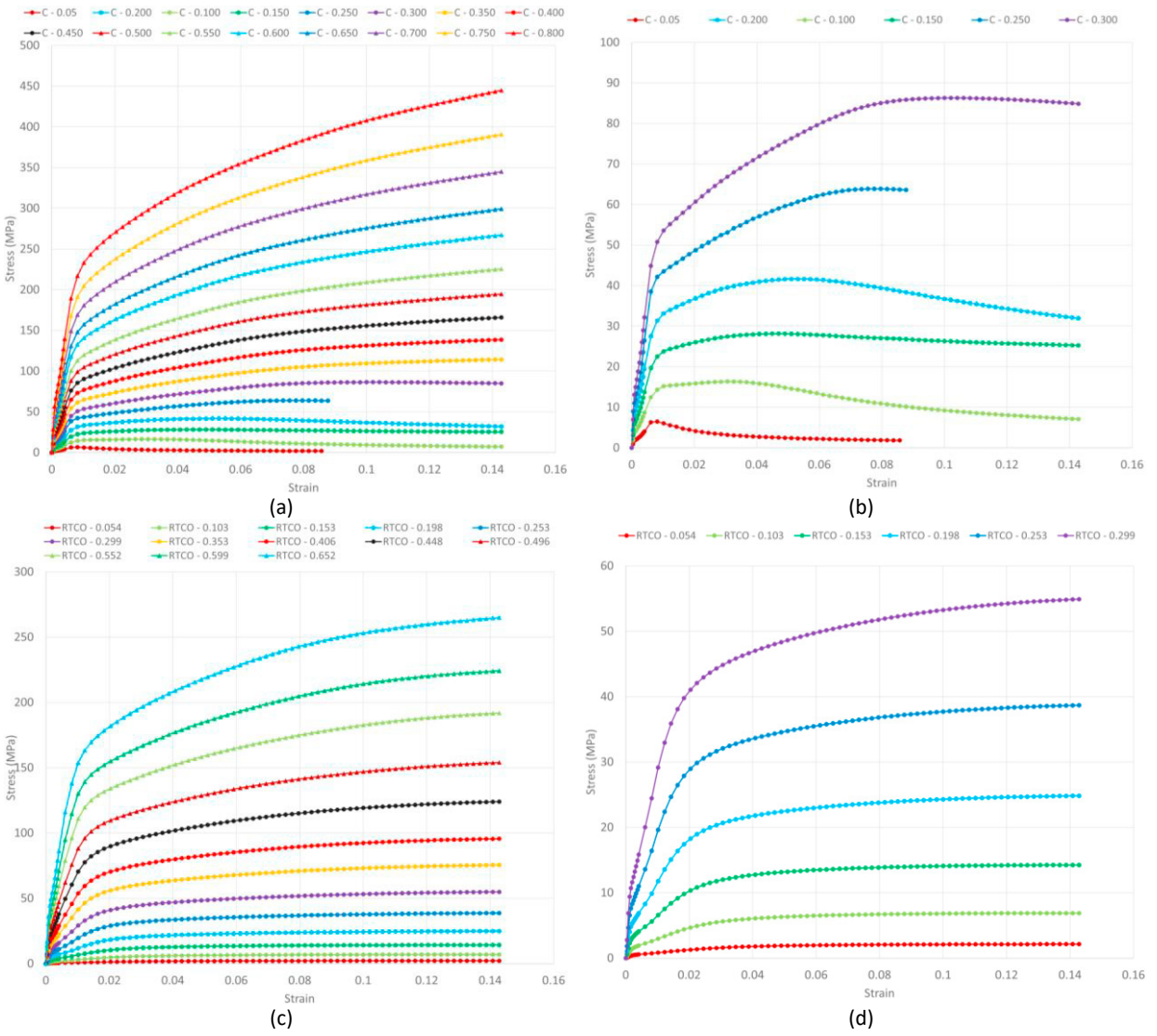

Fig. 4. Stress-strain curves for: (a) cubic cells (all relative densities), (b) cubic cells (low relative density), (c) RTCO cells (all relative densities) and (d) RTCO cells (low relative density).

In figure 4, some of the curves are not exhibited up to the stain of 0.14 because, the structures become locally unstable and Abaqus is not able to converge. This could be fixed with adaptative meshes, but the computational cost would significantly increase. As expected, the ability to withstand loads increases as the density increases [11]. With high density, the results for all cells (even the ones not shown) present stability in their stress-strain curves. However, with low density, C, TC and RCO cells present instabilities while TO and RTCO cells maintain their stable behavior. Fig. 5 shows a 3D image of the von Mises effective stress distribution at the last point of the stress-strain curve for: (a) cubic cells with 5,0% density and (b) with 30,0% density; (c) RTCO cells with 5,4% density and (d) with 29,9% density. The last point of the stress-strain curve represents a strain of 14,29% and it is enough strain to observe the deformation behavior of the structures. Cubic cells are an example of unstable cells at low densities: below 25% density, buckling was observed (Fig. 5 (a)), and above 25% their deformation behavior becomes stable (Fig. 5 (b)). On the other hand, RTCO cells are an example of stable cells both at high and low densities Fig. 5 (c) and (d).

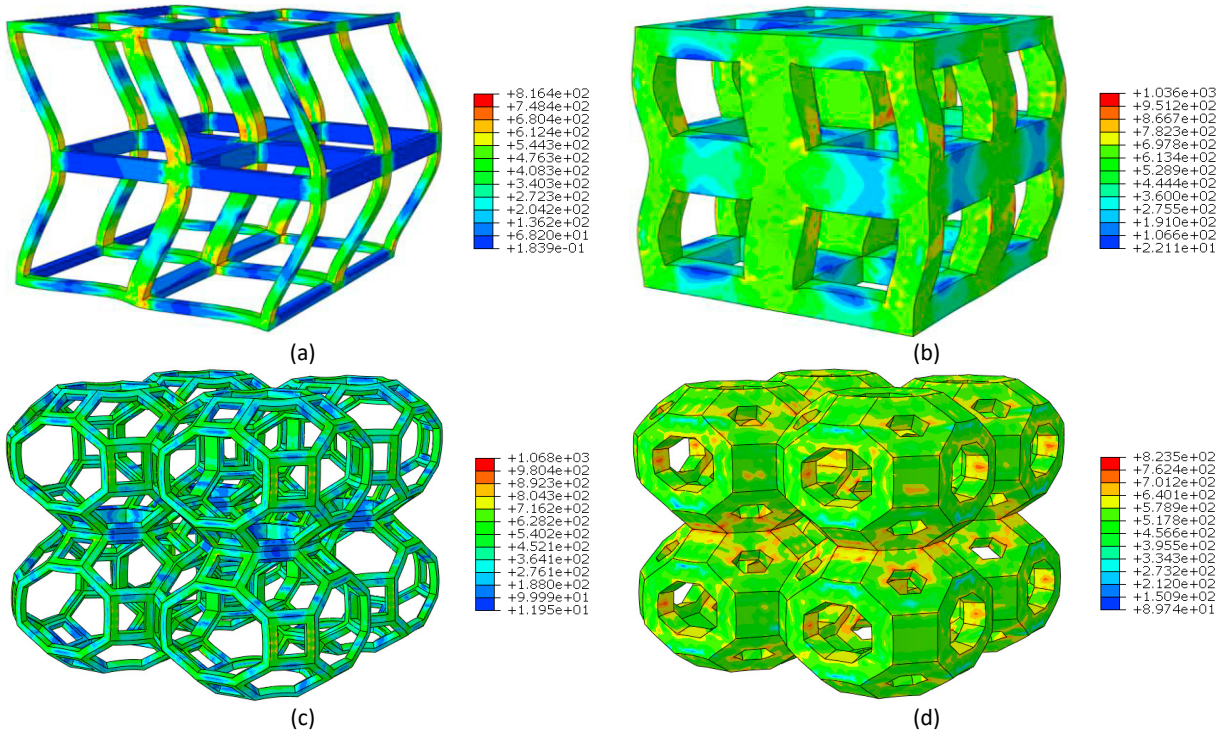

Fig. 5. Von Mises effective stress distribution in MPa at the end of the last point of the compression test for: (a) cubic cells with 5,0% density and (b) with 30,0% density; (c) RTCO cells with 5,4% density and (d) with 29,9% density. Scale factor = 1.

As these structures are intended for temporary implants, it is important that they can reduce stress-shielding by having properties close to the ones of bone. The loss of bone associated with stress shielding can reach very high percentages in structural implants, especially after revision surgeries [17] and can lead to an increased fracture risk [18]. However, the structures are also biodegradable which means that they will lose density (and mechanical capability) as they degrade [19]. To compensate for this effect, the structure employed in a patient may need to be stiffer (with higher density) that the bone replaced in that region. This makes it impossible to eliminate stress-shielding completely but may help reduce it significatively [10].

3.2. Data analysis

The Young's modulus that is intended for these structures is the one of bone, which is very dependent on the bone's density. The bone's density usually varies from 0.03 g/cm^3 [20] to 1.85 g/cm^3 [21] and its Young's modulus is difficult to ascertain. The Young's modulus of bone varies not only with density, but also with age and other metabolic factors [22]. The Young's modulus of cancellous bone with very low density can be as low as 100 MPa to 900 MPa [20,23] and the Young's modulus of cortical bone with very high density can be as high as 20 GPa to 22 GPa [22,24].

The Young's modulus for all relative densities is shown in Table 1. The values for which the several cells are unstable are highlighted with orange and the values for which the Young's modulus is much higher than the required for bone mimicking are highlighted with green.

The data obtained suggests that C, TC and RCO cells cannot reach the lower bound of bone Young's modulus with stability. Additionally, RCO cells also cannot achieve a Young's modulus necessary to mimic cortical bone. Only TO and RTCO cells can reach the whole range of mechanical properties of bone with stability. Relative densities of 60% or above are too high, yielding a Young's modulus that exceeds the necessary to mimic cortical bone.

Table 1 – Young's modulus for every cell and relative density considered. Highlighted with orange: unstable cells. Highlighted with green: cells that present a higher Young's modulus than bone.

C		TO		TC		RCO		RTCO	
$\bar{\rho}$ (%)	E (MPa)	$\bar{\rho}$ (%)	E (MPa)	$\bar{\rho}$ (%)	E (MPa)	$\bar{\rho}$ (%)	E (MPa)	$\bar{\rho}$ (%)	E (MPa)
5.0	1631	5	307	5.1	688	5.0	1104	5.4	210
10.0	3451	10.4	1342	9.9	1948	10.1	2353	10.3	827
15.0	5446	15.4	2887	17.0	4647	15.2	3798	15.3	1893
20.0	7631	20.0	4902	20.3	6082	19.8	5434	19.8	3366
25.0	9261	25.3	7341	25.2	8438	25.3	7649	25.3	5487
30.0	12500	29.7	9823	30.3	11235	29.7	9688	29.9	7902
35.0	15227	34.9	13377	35.6	14412	34.9	12603	35.3	10957
40.0	18188	40.0	17422	39.5	16931	39.7	15446	40.6	13916
45.0	21443	45.0	21932	45.0	20810	45.1	19339	44.8	17935
50.0	24977			49.7	24472			49.6	22090
55.0	28673			54.8	29066			55.2	27356
60.0	33752			59.8	33916			59.9	31735
65.0	37683			65.4	39811			65.2	37430
70.0	43271			70.0	45259				
75.0	49071			75.1	51777				
80.0	55870			79.9	58567				

Fig. 6 presents the same data as Table 1 in a log-log scale and shows in black two additional curves from Gibson and Ashby et al. [14] that represent the bounds for trabecular bone's Young's modulus for two values of the coefficients defined by the authors. The image shows that the curves of the structures are of the same nature of those of bone, i.e., linear in a log-log scale. For relative densities up to 20% the curves of the TO and RTCO structures fall within the bounds of trabecular bone. For relative densities above 20% none of the structures fall within the bounds, however, they come close to them until 25% to 30% relative density. For densities higher than 30%, the curves are expected to diverge from the bounds as the Young's modulus obtained is more like that of cortical bone, instead of trabecular bone. The confluence between the results obtained for TO and RTCO structures and the literature available reinforces the confidence in the results of this study: from those evaluated, TO and RTCO unit cells are the most suitable for bone mimicking as they produce properties like those of bone and are stable in the whole range of density.

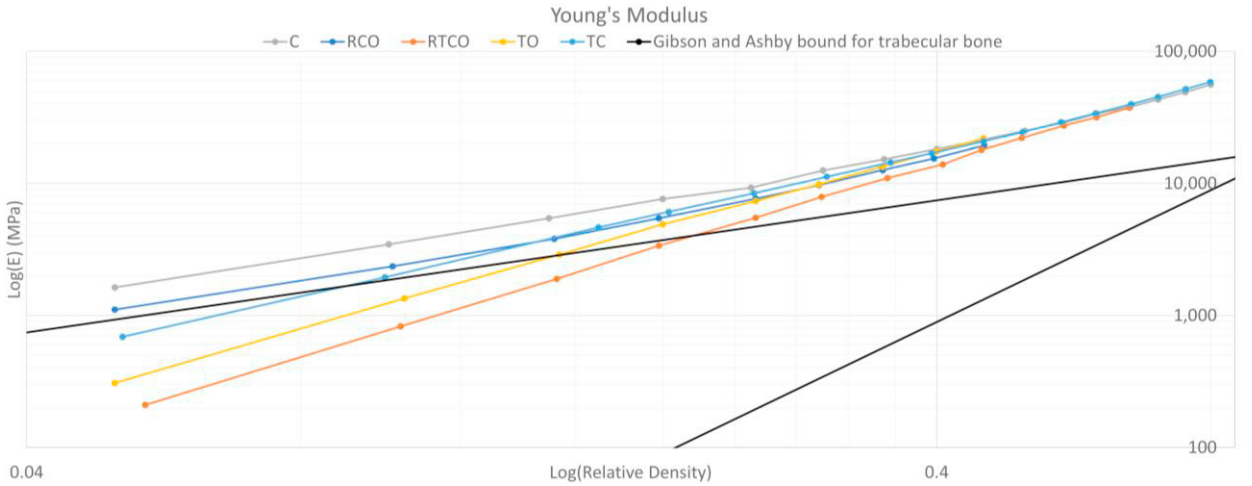

Fig. 6. Young's modulus as a function of density for all cells in a log-log scale. Black – upper and lower bounds for Young's modulus of trabecular bone adapted from Gibson and Ashby et al. [14]

In future works the results will be expanded to 10x10x10 cell arrays instead of 2x2x2, as that is the recommendation of ISO 13314:2011(E) [16]. The numeric models will be validated experimentally with AM specimens. This may help to adjust the inputs to the finite element analyses like the friction coefficient of the AM specimens and the mechanical properties of AM iron, thus further increasing the accuracy of the finite element analysis.

4. Conclusions

A major simulation analysis by finite element modeling was performed, for the first time, on the mechanical stability of cellular lattice arrangements as a function of their relative density. The novelty of the present study is suggesting that for every cell type, that forms a lattice arrangement, there is a range of densities that show a stable mechanical behavior and provide elastic properties that mimic those of trabecular and cortical bone. This density range was identified for Cubic (C), Truncated Octahedron (TO), Truncated Cubic (TC), Rhombicuboctahedron (RCO) and Rhombitruncated Cuboctahedron (RTCO) lattice arrangements. Not all cell types are stable at low relative densities, while for high relative densities, all cells present a stable behavior. Two cell types, TO and RTCO, have demonstrated a strong capability of covering the whole range of Young's modulus that bone exhibits in a stable manner.

Acknowledgements

The authors would like to acknowledge the support provided by Fundação para a Ciência e a Tecnologia of Portugal and IDMEC under LAETA-UID/EMS/50022/2020 and project PTDC/CTM-CTM/3354/2021. The work of Miguel Pinto and Pedro Neves is also greatly acknowledged.

References

[1] Zadpoor AA, Malda J. Additive Manufacturing of Biomaterials, Tissues, and Organs. Ann Biomed Eng 2017;45. https://doi.org/10.1007/s10439-016-1719-y.

[2] Li Y, Jahr H, Lietaert K, Pavanram P, Yilmaz A, Fockaert LI, et al. Additively manufactured biodegradable porous iron. Acta Biomater 2018;77:380–93. https://doi.org/10.1016/j.actbio.2018.07.011.

[3] Sharma P, Pandey PM. Morphological and mechanical characterization of topologically ordered open cell porous iron foam fabricated using 3D printing and pressureless microwave sintering. Mater Des 2018;160:442–54. https://doi.org/10.1016/j.matdes.2018.09.029.

[4] Li Y, Jahr H, Zhou J, Zadpoor AA. Additively manufactured biodegradable porous metals. Acta Biomater 2020;115:29–50. https://doi.org/10.1016/j.actbio.2020.08.018.

[5] Yun Y, Dong Z, Lee N, Liu Y, Xue D, Guo X, et al. Revolutionizing biodegradable metals. Mater Today 2009;12:22–32. https://doi.org/10.1016/S1369-7021(09)70273-1.

[6] Witte F. Biodegradable Metals. Fourth Edi. Elsevier; 2020. https://doi.org/10.1016/b978-0-12-816137-1.00021-0.

[7] Li H, Zheng Y, Qin L. Progress of biodegradable metals. Prog Nat Sci Mater Int 2014;24:414–22. https://doi.org/10.1016/j.pnsc.2014.08.014.

[8] Sharma P, Pandey PM. Corrosion behaviour of the porous iron scaffold in simulated body fluid for biodegradable implant application. Mater Sci Eng C 2019;99:838–52. https://doi.org/10.1016/j.msec.2019.01.114.

[9] Sharma P, Jain KG, Pandey PM, Mohanty S. In vitro degradation behaviour, cytocompatibility and hemocompatibility of topologically ordered porous iron scaffold prepared using 3D printing and pressureless microwave sintering. Mater Sci Eng C 2020;106:110247. https://doi.org/10.1016/j.msec.2019.110247.

[10] Benedetti M, du Plessis A, Ritchie RO, Dallago M, Razavi SMJ, Berto F. Architected cellular materials: A review on their mechanical properties towards fatigue-tolerant design and fabrication. Mater Sci Eng R Reports 2021;144:100606. https://doi.org/10.1016/j.mser.2021.100606.

[11] Ahmadi SM, Yavari SA, Wauthle R, Pouran B, Schrooten J, Weinans H, et al. Additively manufactured open-cell porous biomaterials made from six different space-filling unit cells: The mechanical and

morphological properties. Materials (Basel) 2015;8:1871–96. https://doi.org/10.3390/ma8041871.
[12] Chantarapanich N, Puttawibul P, Sucharitpwatskul S, Jeamwatthanachai P, Inglam S, Sitthiseripratip K. Scaffold library for tissue engineering: A geometric evaluation. Comput Math Methods Med 2012;2012. https://doi.org/10.1155/2012/407805.
[13] Li Y, Lietaert K, Li W, Zhang XY, Leeflang MA, Zhou J, et al. Corrosion fatigue behavior of additively manufactured biodegradable porous iron. Corros Sci 2019;156:106–16. https://doi.org/10.1016/j.corsci.2019.05.003.
[14] Gibson LJ, Ashby MF. Cellular solids. vol. 22. Second. 1997. https://doi.org/10.1016/0021-9290(89)90056-0.
[15] E9-19 ASTM Standard Test Methods of Compression Testing of Metallic Materials at Room Temperature. West Conshohocken, PA: 2019. https://doi.org/10.1520/E0009-19.2.
[16] International Organization for Standardization. ISO 13314:2011 Mechanical testing of metals – Ductility testing – Compression test for porous and cellular metals (ISO Standard No. 13314:2011(E)). Int Organ Stand 2011;2011:1–7.
[17] Nogueira P, Folgado J, Quental C, Gamelas J. Metaphyseal sleeves in revision total knee arthroplasties : Computational analysis of bone remodeling. Knee 2022;37:10–9. https://doi.org/10.1016/j.knee.2022.05.006.
[18] Gundry M, Hopkins S, Knapp K. A Review on Bone Mineral Density Loss in Total Knee Replacements Leading to Increased Fracture Risk. Clin Rev Bone Miner Metab 2017;15:162–74. https://doi.org/10.1007/s12018-017-9238-4.
[19] Sharma P, Pandey PM. Corrosion rate modelling of biodegradable porous iron scaffold considering the effect of porosity and pore morphology. Mater Sci Eng C 2019;103:109776. https://doi.org/10.1016/j.msec.2019.109776.
[20] Røhl L, Larsen E, Linde F, Odgaard A, Jørgensen J. Tensile and compressive properties of cancellous bone. J Biomech 1991;24:1143–9. https://doi.org/10.1016/0021-9290(91)90006-9.
[21] Karageorgiou V, Kaplan D. Porosity of 3D biomaterial scaffolds and osteogenesis. Biomaterials 2005;26:5474–91. https://doi.org/10.1016/j.biomaterials.2005.02.002.
[22] McCalden RW, McGlough JA, Barker MB, Court-Brown CM. Age-related changes in the tensile properties of cortical bone. The relative importance of changes in porosity, mineralization and microstructure. J Bone Jt Surg - Ser A 1993;75:1193–205. https://doi.org/10.2106/00004623-199308000-00009.
[23] Linde F, Gothgen CB, Hvid I, Pongsoipetch B. Mechanical properties of trabecular bone by a non-destructive compression testing approach. Eng Med 1988;17:23–9. https://doi.org/10.1243/EMED_JOUR_1988_017_008_02.
[24] Öhman C, Baleani M, Pani C, Taddei F, Alberghini M, Viceconti M, et al. Compressive behaviour of child and adult cortical bone. Bone 2011;49:769–76. https://doi.org/10.1016/j.bone.2011.06.035.